# 8

# High-Density Nickel Nanowire Arrays

Kornelius Nielsch[1], Riccardo Hertel[2] and Ralf B. Wehrspohn[3]
[1] *Max-Planck-Institute of Microstructure Physics, Weinberg 2, 06120 Halle, Germany*
*knielsch@mpi-halle.de*
[2] *Institute of Solid State Research (IFF) Research Center Jülich, D-52425 Jülich, Germany,*
*r.hertel@fz-juelich.de*
[3] *Department of Physics, University Paderborn, 33095 Paderborn, Germany*
*wehrspohn@physik.upb.de*

## 8.1. INTRODUCTION

The application of ferromagnetic-material-filled ordered matrices for perpendicular magnetic storage media is becoming increasingly relevant to extend the areal density of magnetic storage media beyond the predicted superparamagnetic limit ($>70$ Gbit/in$^2$) [1,2]. One bit of information corresponds to one single-domain nanosized particle or so-called nanomagnet. Since each bit would be composed of a single large aspect particle, the areal density of pattered media can, in principle, be much more than an order of magnitude higher than that in conventional longitudinal media. For example, an areal density of about 1 Tbit/in$^2$ can be achieved by a hexagonally arranged array of nanomagnets with a lattice constant of about 25 nm.

The fabrication of nanomagnet arrays based on hexagonally arranged porous alumina as a template material is cheaper than that based on traditional fabrication methods such as nanoscaling using electron beam lithography [3]. Moreover, these arrays of magnetic nanowires can be easily fabricated over areas of several cm$^2$. Since 1981, several articles on unarranged porous alumina templates filled with ferromagnetic materials have been published [4–8]. These structures have large size distributions of the pore diameter and interpore distance, and the filling degree of the pores is not specified. On the basis of an approach by Masuda [9] (see also Chapter 3), we have shown that ordered porous alumina arrays with a sharply defined pore diameter and interpore distance can be obtained by a two-step electrochemical anodization process of aluminium [10,11]. The degree of self-ordering is polydomain with a typical domain size of a few micrometres.

Monodomain pore arrays can be obtained by electron-beam lithography [12] or imprint technology [13].

## 8.2. EXPERIMENTAL DETAILS

### *8.2.1. Preparation of the Porous Alumina Structure*

The hexagonally ordered porous alumina membranes were prepared via a two-step anodization process, which is described in detail elsewhere [13,14]. A first long-time anodization caused the formation of channel arrays with a high aspect ratio and regular pore arrangements via self-organization [9–14]. After complete dissolution of the oxide structure (Figure 8.1a), the surface of the aluminium substrate kept the regular hexagonal texture of the self-organized pore tips, which act as a self-assembled mask for a second anodization process. After a second anodization for 1 hour, an ordered nanopore array (Figure 8.1b) was obtained with straight pores from top to bottom and a thickness of typically 1 μm. The parameters are 0.3 M oxalic acid, $U_{\text{ox}} = 40$ V and $T = 2\,^{\circ}$C.

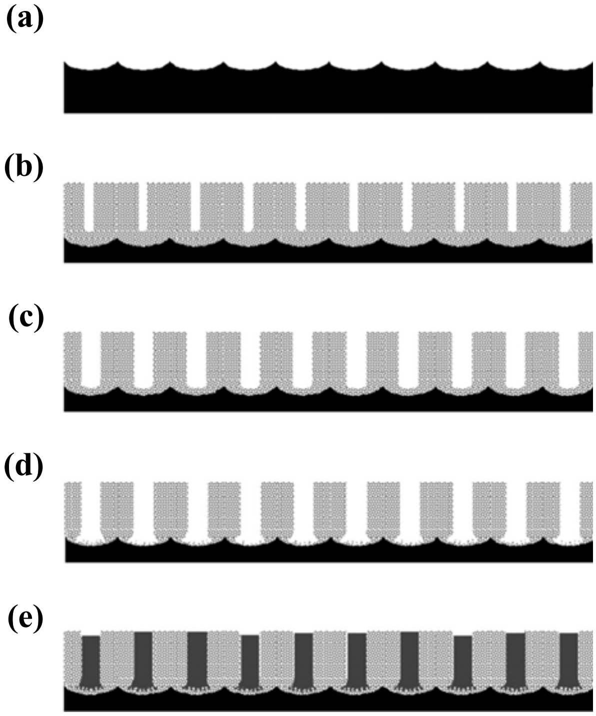

FIGURE 8.1. Schematic diagram demonstrating the fabrication of a highly ordered porous alumina matrix and the preparatory steps necessary for the subsequent filling of the structure. The Al-substrate was pre-structured by a long-time anodizsation and by removing the oxide (a). A second anodizsation step yielded a highly ordered alumina pore structure (b). The barrier layer was thinned and the pores were widened by isotropic chemical etching (c). To thin the barrier layer further, two current-limiting anodizsation steps followed, with dendrite pores forming at the barrier layer (d). Pulsed electrodeposition of nickel in the pores is shown in (e).

Thinning of the barrier layer improves the quality and homogeneity of the deposition process in the pores significantly. The barrier layer can be thinned by chemical pore widening and by current-limited anodization steps: Firstly, the oxalic acid was heated up to 30 °C to decrease the thickness of the barrier layer by chemically widening the pores (Figure 8.1c). After 3 hours, for example after 3h pore widening, the barrier layer was decreased from 45 to 30 nm and the mean pore diameter was increased to approximately 50 nm. Afterwards, the electrolyte was cooled down to 2 °C to interrupt the widening process.

Secondly, the structure was anodized twice for 15 minutes using constant current conditions of 290 and 135 $\mathrm{mA/cm^2}$, respectively. During these anodization steps, the anodization potential decreased, the pores branched out at the formation front and the thickness of the barrier layer was reduced significantly. Finally, the anodizing potential reached a value of 6–7 V, which corresponds to a barrier oxide thickness of less than 10 nm. A detailed description of the pretreatment of the porous alumina structure for the filling process of the pores has been published recently [14].

### *8.2.2. Filling of the Pores with Magnetic Materials*

Nickel and cobalt were electrodeposited from an aqueous electrolyte at the pore tip of our high-aspect-ratio porous material (Figure 8.1e). Both metals were deposited from a highly concentrated Watts-bath electrolyte to achieve a high concentration of metal ions in each pore. The ingredients for nickel electrolyte is given as follows: 300 g/l $NiSO_4 \cdot 6H_2O$, 45 g/l $NiCl_2 \cdot 6H_2O$, 45 g/l $H_3BO_3$, pH = 4.5. The mixture for the cobalt deposition is written in a similar manner and it has a pH value of 4.3. The electrolyte temperature is 35 °C.

Frequently, an alternating current (ac) signal is used for the deposition [1,2,5,7,15–17] when the porous alumina structure is kept on its aluminium substrate for the filling process. The metal is directly deposited upon the nearly isolating oxide barrier layer at the pore tips. Recently we have demonstrated that a pulsed electrodeposition concept (PED) is more suitable for a direct and homogeneous filling of the porous alumina structures. Here, only a short technical description is given.

The pore filling was based on modulated pulse signals in the ms-range. During the relatively long pulse of negative current (8 ms, $I_{\mathrm{pulse}} = -70\ \mathrm{mA/cm^2}$) the metal is deposited on the pore ground. The measured voltage signal varies between −8 and −12 V. After the deposition pulse, a short pulse of positive polarization (2 ms, $U_{\mathrm{pulse}} = +4\mathrm{V}$) follows to interrupt the electric field at the deposition interface immediately. The relative long break time (0.3 to 1s) was allowed between the deposition pulses to refresh the ion concentration at the deposition interface, to let disappear the deposition by-products from the pore tips and to ensure a stable pH value in each pore during the deposition. Consequently, the delay time $t_{\mathrm{off}}$ improves the homogeneity of the deposition. For the deposition of nickel a $t_{\mathrm{off}} = 990$ ms was selected. The deposition was continued up to the beginning of the metal deposition on top of the matrix structure.

### *8.2.3. Characterization of the Filling Material*

For the characterization of the metal-filled template and its magnetic properties, the top of the template structure was fixed to a silicon substrate by conducting glue. Next, the

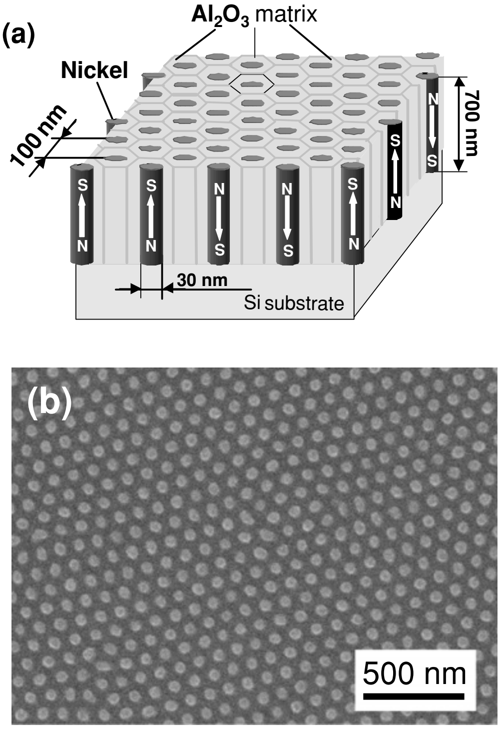

FIGURE 8.2. (a) Sketch of the magnetic structure. Nickel nanowires are arranged in a hexagonal array perpendicular to a silicon substrate and embedded in an aluminium oxide matrix. (b) Top-view SEM micrograph of a nickel-filled alumina matrix, with an interpore distance of 105 nm, fixed on a silicon substrate. The Ni columns have a diameter $D_P = 35$ nm and a length of ~700 nm.

aluminium substrate was removed by a saturated solution of HgCl and the structure was turned upside down. After removing from the top an ≈200-nm-thick layer of the filled template by a focused ion beam, which was estimated from the thinning rate, the top ends of the nanowires became visible at the surface and a relatively smooth surface was obtained.

As an example, Figure 8.2b shows an SEM image of a nickel sample with a nanowire diameter of 35 nm and 105 nm interpore distance. The ferromagnetic nanowires (white) with a monodisperse diameter are embedded in the porous alumina matrix (black). Because of the self-organization process, the nanowires are arranged in a hexagonal pattern. Figure 8.3 shows an SEM image of sample (B). The ferromagnetic nanowires (white) are embedded in the porous alumina matrix (black). Because of the self-organization process, the nanowires are hexagonally arranged with an interwire distance of 100 nm. Sample (B) has a wire diameter of approximately 35 nm. Nearly 100% pore filling was obtained for all three samples discussed, demonstrating that the metallic filling extends over the whole length of the pore [14]. The crystallinity of these samples was further analyzed by X-ray diffraction (XRD).

From the 2ϑ-scan, the average crystallite size is estimated using the Scherrer equation for round particles, yielding an average grain size $D_{Gr} = 10$–$15$ nm.

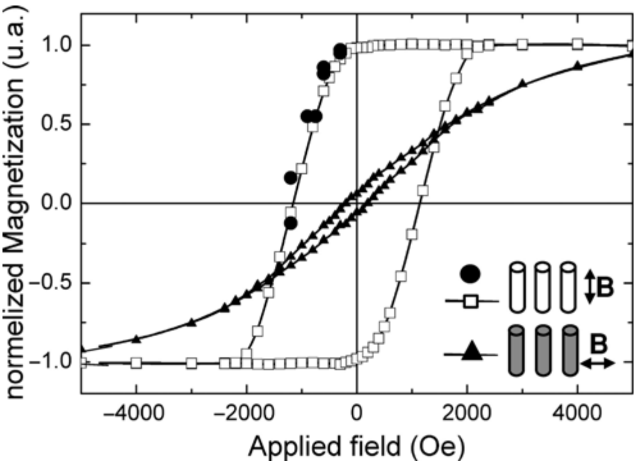

FIGURE 8.3. SQUID-hysteresis loops of the nickel nanowire array with a pitch of 105 nm, a column length of about 700 nm and a wire diameter of 30 nm measured with an applied field parallel (□) and perpendicular (▲) to the column axis. Results from MFM investigations (●) while an external magnetic field $H_{ex}$ was applied to the sample (analyzed statistically treated).

## 8.3. MAGNETIC PROPERTIES OF NICKEL NANOWIRE ARRAYS

The bulk magnetic properties of the highly ordered array with high-aspect-ratio magnetic columns (length/diameter ~25) were investigated by SQUID-magnetometer measurements. Figure 8.3 shows the bulk magnetization hysteresis loops for the nickel array measured with an applied field parallel and perpendicular to the wire axis.

The hysteresis loops measured for the nickel nanowire (Figure 8.3) array with the magnetic field applied parallel to the wire axis show a coercive field of $H_C^{||} = 1200$ Oe and a squareness of nearly 100%. The measured coercive fields for the hysteresis loops measured perpendicular to the wire are $H_C^{\perp} \approx 150$ Oe and drastically smaller than $H_C^{||}$. This sample has a preferential magnetic orientation along the wire axis. Here, we give only a short description of the analysis of the sample. A detailed analysis of the influence of the nanowire diameter on the bulk-magnetic properties of hexagonally ordered 100 nm period nickel nanowire arrays can be found in [18]. The total magnetic anisotropy of this sample is influenced by the magnetic anisotropy resulting from the shape of the Ni nanowires ($H_S = 2\pi M_S = 3200$ Oe) and the dipole or so-called demagnetization fields ($H_D^{||} = \pi^2 M_S D_P^2 c \approx 550$ Oe; $c$: pore density) between the nanowires. The magnetocrystalline anisotropy of the nano-crystalline Ni wires gives only a small contribution ($H_K = 2K_1/M_S = 195$ Oe) at room temperature. The Ni nanomagnets are single-domain particles. Their magnetic reversal process occurs by inhomogeneous switching modes, as discussed in the micromagnetic modelling Section 8.5 and [19]. The small size distribution of the pore diameter ($\Delta D_P/D_P < 10\%$) [9,11] has a positive impact on the magnetic properties. Here, we report the highest measured coercive fields $H_C$ of about 1200 Oe for a close-packed nickel nanowire array embedded in a membrane matrix. Previous works on unarranged nickel nanowire arrays show lower coercive fields of about 1000

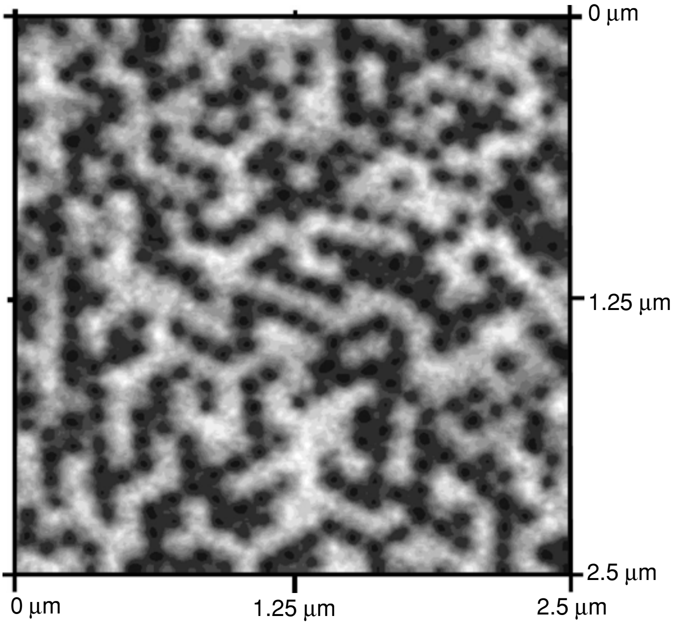

FIGURE 8.4. Magnetic force microscopic image of the highly ordered nickel nanowire array with a pitch of 105 nm embedded in the alumina matrix in the demagnetized state, showing the magnetic polariszation of the pillars alternately “up” (white) and “down” (black).

Oe or less in the preferential magnetic orientation [8,20]. The large size distribution (up to $\Delta D_P/D_P > 50\%$) [7] of the pore diameters and the interwire distance enhance the magnetic interactions in the nanowire arrays and reduce the squareness of the hysteresis loop.

In contrast, the MFM image reflects the magnetic polarization at the top end of each magnetic nanowire. Figure 8.4 demonstrates the domain structure of an array of nickel columns in the demagnetized state. The geometric parameters of the sample are the same as for Figure 8.1b. Dark spots in the magnetic image imply the magnetization pointing up and a bright spots imply the magnetization pointing down. Up magnetization may be interpreted as a binary “1” and down magnetization as a binary “0”. It can be deduced from the picture that the Ni pillars are single-domain nanomagnets aligned perpendicular to the surface. The patterned domain structure is due to an antiferromagnetic alignment of pillars influenced by the weak magnetic interaction between these nanomagnets. The labyrinth pattern (Figure 8.4) of the domain structure is characteristic for hexagonally arranged single-domain magnetic particles with a perpendicular magnetic orientation in the demagnetized state. In the case of a quadratic lattice, each of the four nearest neighbours will be aligned anti-parallel and the domain structure exhibits a checkerboard pattern [2]. In the hexagonal lattice, two of the six nearest neighbours will align their magnetization parallel and four will be magnetized anti-parallel, if the stray field has only nearest-neighbour interaction. In Figure 8.4, we observe that in average 2.5 nanomagnets are aligned parallel and that 3.5 are magnetized anti-parallel. We suppose that the stray

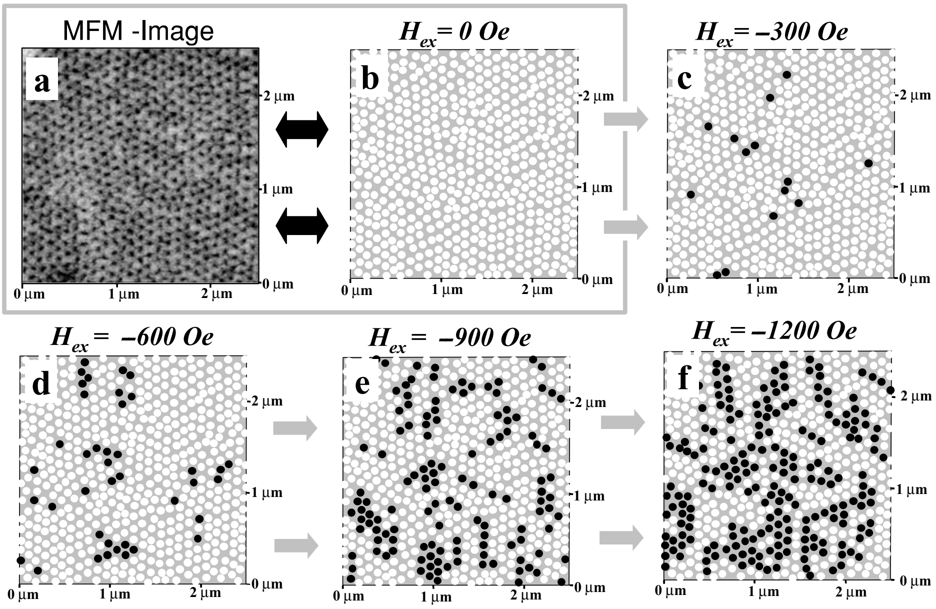

FIGURE 8.5. An external magnetic field was applied perpendicular to the sample surface. (a) The MFM image of the completely magnetizsed nanowire array. The MFM image (a) was enhanced numerically: (a)→(b). Numerically enhanced MFM images recorded with an applied magnetic field of $H_{\text{ex}} = -300$ Oe (c), –600 Oe (d), –900 Oe (e) and –1200 Oe (f).

field interaction is extended over several lattice periods $D_{\text{int}}$, due to the high aspect ratio of the magnetic nanowire.

Additionally, MFM investigations with applied magnetic field were carried out on the sample to study the switching behaviour of the individual nanowires in the array. A low moment magnetic tip was used for the MFM scan, in order to prevent switching of the magnetization in the nanowires by the dipole field of the magnetic tip ($H_{\text{tip}} \approx 50$ Oe). Before this investigation, the sample was completely magnetized by an external magnetic field of about 5000 Oe along the wire axes. The first scan was performed without an external field, see Figure 8.5a. In order to get a better impression about the magnetic polarization of each pillar the MFM images were numerically enhanced (Figures 8.5a →and 8.5b). There are no differences in the magnetic polarization between the magnetic pillars (Figure 8.5a) and in the enhanced image every nanowire shows a positive polarization (white dots). Because of the fact that the applied field $H_{\text{ex}}$ was larger than the saturation field $H_{\text{S}}^{\|}$ and that the hysteresis loop has a magnetic squareness of about 100%, we may deduce that the magnetization in each pillar of the array is oriented in one direction (up or down). Even though $H_{\text{ex}} = 0$ Oe and the maximum demagnetization field of $H_{\text{D}} = -550$ Oe is achieved, the structure remains in the saturated state. During the following MFM scans an increased external magnetic field is applied in the direction opposite to the magnetization. The numerically enhanced images are shown for $H_{\text{ex}} = -300$ Oe (Figure 8.5c), $-600$ Oe (Figure 8.5d), $H_{\text{ex}} = -900$ Oe (Figure 8.5e) and $H_{\text{ex}} = -1200$ Oe (Figure 8.5f). When the external field is increased the effective field in the sample increases: $H_{\mathrm{eff}} = H_{\mathrm{D}} + H_{\mathrm{ex}}$. For Figure 8.5c an average effective field of about 850 Oe is obtained. Because of fluctuations of the local dipole fields and the switching fields of the individual nanowires, a few magnetic particles reverse their magnetization (black dots) also in the case $H_{\mathrm{eff}} < H_{\mathrm{C}}^{\|}$. Increasing the external field leads to an increasing number of reversed magnetized pillars (Figures 8.5b–8.5f). The enhancement of $H_{\mathrm{eff}}$ is partly compensated by the reduced dipole interactions from the reversed pillars. In the final image (Figure 8.5f) the applied external field has reached the coercive field $H_{\mathrm{C}}^{\|\|} =$ 1200 Oe. The number of switched (black) and unswitched (white) nanowires are nearly equal. In this case the average demagnetization field in the sample will be reduced nearly to a minimum and $H_{\mathrm{ex}} \approx H_{\mathrm{eff}} \approx H_{\mathrm{C}}^{\|}$. Additionally our MFM images were statistically analyzed and compared with the data from the measured hysteresis loop in the preferential magnetic orientation, see Figure 8.3 ($H_{\mathrm{ex}}$ || wire). With a few fluctuations the MFM analysis corresponds very nicely to the bulk magnetic characterization of the sample.

In order to examine in more detail the suitability of this nickel nanowire array for patterned perpendicular magnetic media, we have tried to completely magnetized a defined area of a demagnetized sample by a strong magnetic MFM tip ($H_{\mathrm{tip}} \approx 250$ Oe) and an external magnetic field ($H_{\mathrm{ex}} = -1200$ Oe). The amount of the applied external field was nearly equal to the average switching field ($H_{\mathrm{sw}}$) of the individual nanowire ($H_{\mathrm{sw}} \approx H_{\mathrm{C}}^{\|} = 1200$ Oe) and was applied in the direction of the nanowire axis. Starting in the upper region of Figure 8.6 the strong magnetic tip was scanned over an area of $5 \times 5\ \mu\mathrm{m}^2$. Hereby, a total external field of about $H'_{\mathrm{ex}} = H_{\mathrm{ex}} + H_{\mathrm{tip}} = -1450$ Oe was

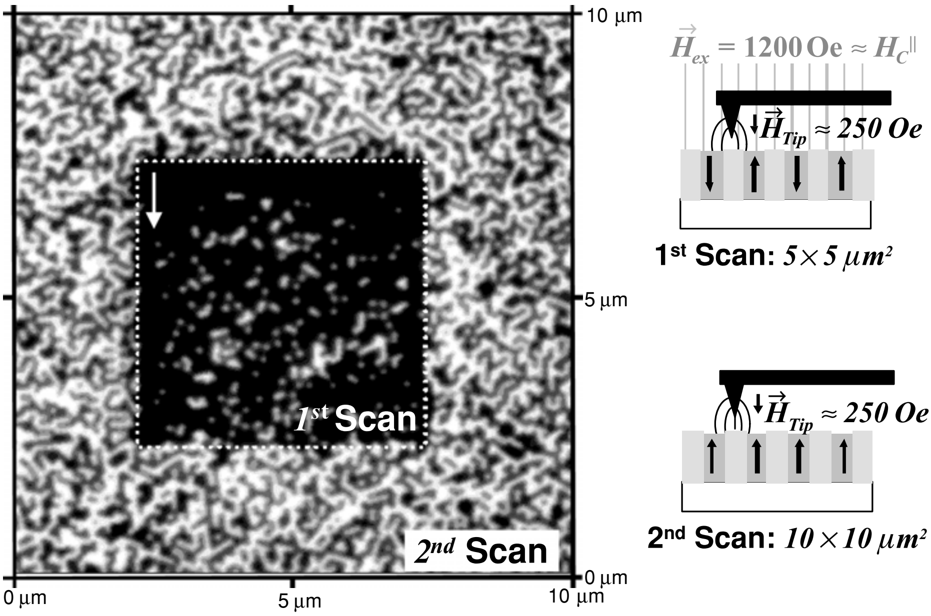

FIGURE 8.6. Local magnetic switching of a demagnetized sample area ($5 \times 5\ \mu\mathrm{m}^2$, 1st scan) by a strong magnetic MFM tip ($H_{\mathrm{tip}} \approx 250$ Oe) and an external magnetic field ($H_{\mathrm{ex}} = -1200$ Oe). This image of the domain pattern ($10 \times 10\ \mu\mathrm{m}^2$) was recorded by a second subsequent MFM scan without an external magnetic field.

applied locally to the tips of the nickel nanowires. Subsequently, the external magnetic field was switched off. An enlarge area of 10 × 10 $\mu m^2$ (Figure 8.6) was scanned with the magnetic tip in order to measure the domain pattern of the manipulated area in the nanowire array. Inside the area of the first scan nearly every nickel column (~93%) is magnetized in the same direction.

Figure 8.6 shows the local impact (dark quadratic region) of the external magnetic field and the strong magnetic tip during the first MFM scan on the magnetization of nanowires. Around the magnetized region of 5 × 5 μm the nickel nanowire array remained in the demagnetized state and exhibited the labyrinth-like domain pattern (Figure 8.4). The border between the magnetized area and the surrounding demagnetized area is clearly visible. From the picture, it can be concluded that the applied magnetic field ($H_{sw} \approx H_C^{\|}$) alone was not strong enough for the switching of magnetic polarization in the Ni columns Hence, the additional field contribution form the strong MFM tip ($H_{tip}$) enabled the local switching process in the Ni nanowire array.

The probability for a nickel nanowire to remain unswitched (light spots) increases in the lower region of the magnetically manipulated area (Figure 8.6, 1st scan). In the upper region, where the first magnetic scan procedure had started, the first five or six horizontal nanowire rows have been completely magnetized in the same direction. During the first scan procedure when the area of the completely magnetized nanowires was growing, the probability for nanomagnet to remain unswitched increased. We assume that the stray field interactions between the demagnetized and the magnetized area can be neglected and the net stray field in the demagnetized area is zero. By increasing the area of parallel magnetized nanowires the dipole interactions between the magnetic elements are enhanced and the applied local field ($H_{tip} + H_{ex}$) is getting less sufficient for a complete magnetic alignment of magnetization in a horizontal row of nickel columns. At the left and right border of the magnetically manipulated area the stray field interactions are weak and a lower number of unswitched magnetic columns is observed there. From this experiment, it can be concluded that the stray field dipole interactions between the nanowires are extended over several interwire distances due to their high aspect ratio (nanowire length to interwire distance: $L/D_{INT} \approx 7$). In principle, the single nanowire can store one bit of information and can be locally switched independently to the magnetization of its nearest neighbours.

## 8.4. NICKEL NANOWIRE ARRAYS WITH 2D SINGLE CRYSTALLINE ARRANGEMENT

By using imprint lithography as a tool for the pre-pattering of the aluminium surfaces, alumina templates with a perfect hexagonal pore arrangement on a $cm^2$-scale can be achieved by a single anodization process. For the first time, Masuda *et al.* [13] has used this technique for fabrication of perfectly ordered and unfilled alumina membranes on a small scale. In this chapter, the fabrication of Ni nanowire arrays on a $cm^2$-scale based on imprint lithography will be presented.

For the sample preparation, mechanically polished Al substrates were patterned by an imprint master mould described elsewhere [15]. The stamp consists of hexagonal arrays of $Si_3N_4$ pyramids with a pitch of $a = 500$ nm (Figure 8.7a). The imprinted etch

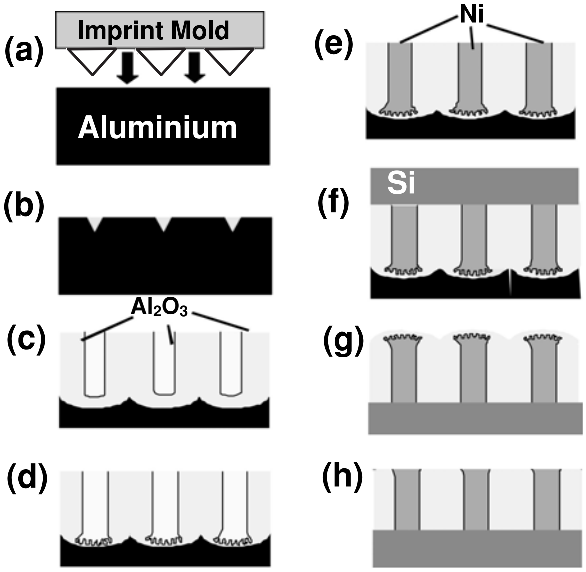

FIGURE 8.7. Preparation steps for fabrication of nickel nanowire arrays embedded in a perfectly arranged alumina matrix, which is fixed to a Si substrate. See the text for details.

pits on the Al surface act as nucleation sides for the pore formation (Figure 8.7b). The pre-structured Al surface was anodized with 1 wt.% $H_3PO_4$ at 195 V for 75 minutes. Alumina templates (Figure 8.7c) with a perfect hexagonal arrangement of pore channels on a $cm^2$-scale were obtained. Subsequently, the barrier layer was thinned at the pore bottom (Figure 8.7d) from about 250 nm down to less than 7 nm, which results in the formation of small dendrite pores at the pore bottom. Nickel was directly plated onto the nearly insulating barrier by current pulses (Figure 8.7e) and a nearly 100% pore filling was obtained. Subsequently, Si substrates were fixed on top of the area (Figure 8.7f), the Al substrate was selectively removed by chemical etching and the sample was turned upside down (Figure 8.7g). Finally, the barrier layer and the dendrite part of the nanowires were removed by etching with a focused ion beam (Figure 8.7h), in order to reduce the stray field interactions between the nanowires. Scanning electron images (Figure 8.8a) of the nanowire structure revealed $h \approx 4\ \mu m$, $a = 500\,nm$ and $D_P = 180\,nm$ with a dispersity $\Delta D_P/D_P < 2\%$. In comparison, Figure 8.8b shows a nickel nanowire arrays with 2D-polycrystalline arrangement of the nanowires. This nanowire array has a medium range ordering and a larger dispersity $\Delta D_P/D_P \approx 10\%$ and was fabricated by the classical two-step anodization process. Both samples were fabricated under identical electrochemical conditions.

The hysteresis loops were measured for both samples in the direction of and perpendicular to the nanowire axis (Figure 8.9). In the case when the nanowires have a monodisperse pore diameter and monocrystalline arrangement, a coercive field of 250 Oe and a remanence of 42% were detected. Because of larger dipolar interaction in the nanowire array, based on the larger deviation of the nanowire diameter and the higher disorder of the magnetic array, the second sample exhibits a reduced coercivity

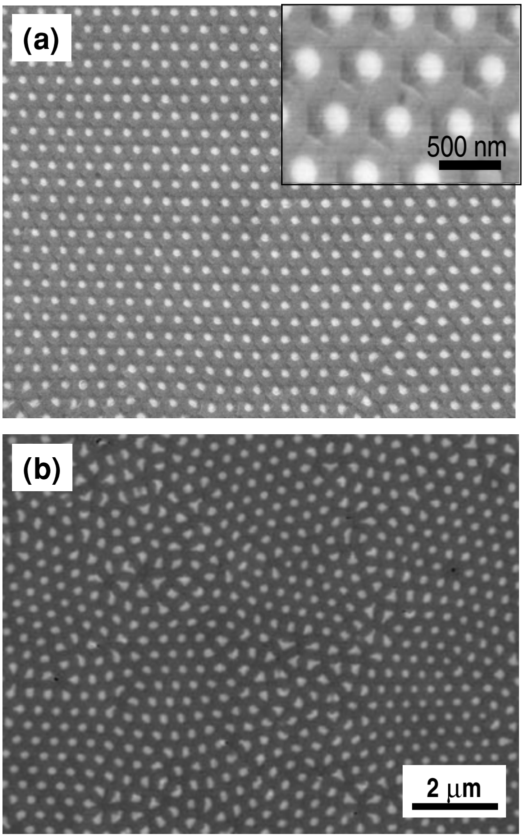

FIGURE 8.8. SEM micrographs of nickel nanowire arrays with a 2D-monocrystalline (a) and 2D-polycrystalline (b) arrangement of the magnetic columns fabricated by imprint lithography (a) and self-organization (b), respectively. Both arrays have 500 nm interwire distance and 180 nm column diameter. The length of the magnetic columns is ~5 μm. The inset in (a) shows a higher magnification of the same Ni nanowire array with the perfect arrangement.

of 160 Oe and a remanence of 30%. In contrast to our earlier results on Ni nanowire with $D_\mathrm{P} < 55$ nm [4], a single Ni nanowire with $D_\mathrm{P} = 180$ nm diameter does not exhibit a box-like magnetization loop. We believe that the reduced remanence of an array of nanowires is due to dipolar interactions and the sample with the 2D-monocyrstalline arrangement (Figure 8.8a) has a narrower distribution of the nanowire switching fields $(\Delta H_\mathrm{sw}/H_\mathrm{sw} \approx 2\Delta D_\mathrm{P}/D_\mathrm{P})$.

## 8.5. MICROMAGNETIC MODELLING

A microscopic description of the magnetic properties of small ferromagnetic particles can be obtained in the framework of micromagnetism [21,22]. The theory of micromagnetism provides the mathematical background for the calculation of magnetic structures in ferromagnets. Micromagnetism is a continuum theory in which the

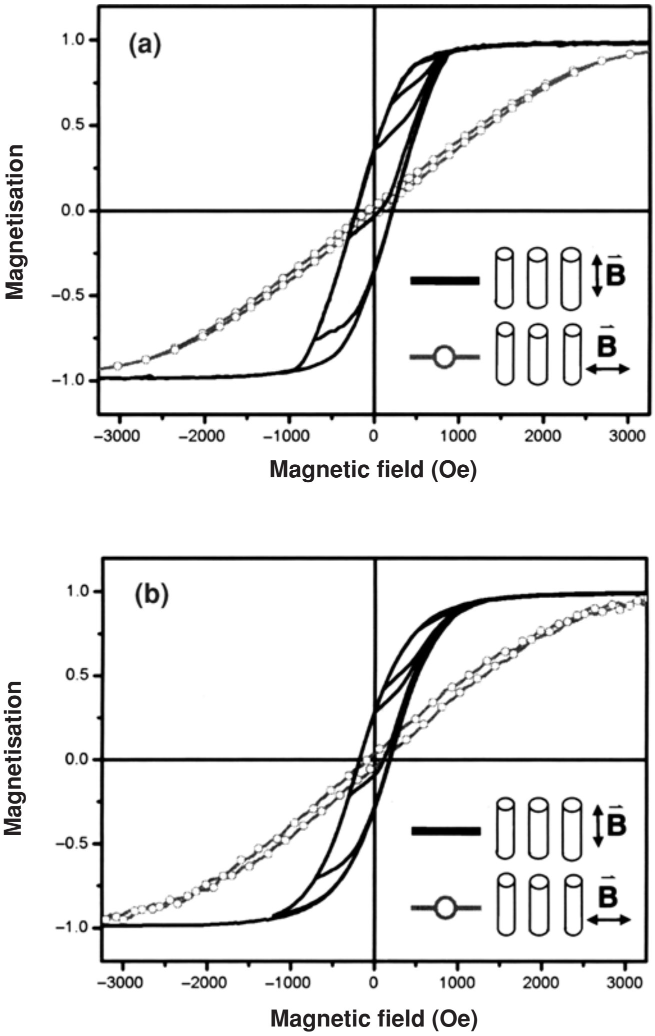

FIGURE 8.9. SQUID-hysteresis loops of the nickel nanowire arrays with a 2D-monocrystalline (a) and 2D-polycrystalline (b) arrangement measured with an applied field parallel and perpendicular to the column axis.

magnetic structure is described as a directional vector field of the magnetization $\boldsymbol{M}(\boldsymbol{r})$ or the polarization $\boldsymbol{J}(\boldsymbol{r}) = \mu_0 \boldsymbol{M}(\boldsymbol{r})$ in the sample. In principle, all the macroscopic magnetic quantities, such as the remanence, the susceptibility or the coercive field, can be obtained from this vector field if it is known as a function of space and time. Micromagnetic studies allow for a detailed analysis of the magnetic structure and magnetization processes, so that they give insight into magnetism on length scales and time scales which are experimentally difficult to access. The combination of experimental measurements and micromagnetic studies enables a deeper and broader understanding of magnetization processes and magnetic properties of nanostructures.

### *8.5.1. Basics of Micromagnetism*

A fundamental principle of micromagnetism is that the energy of a magnet depends on the magnetic structure ***M(r)*** in the sample. Usually, it is sufficient to consider the following four contributions to the micromagnetic energy density $e(\boldsymbol{r})$:

1. The exchange energy density $e_{\mathrm{exc}} = A \times [(\nabla m_x)^2 + (\nabla m_y)^2 + (\nabla m_z)^2]$ describes the tendency of a ferromagnet to maintain a local ordering of the magnetization by aligning neighbouring magnetic moments parallel to each other. The exchange constant $A$ is a material parameter that describes the strength of the exchange interaction, and $\boldsymbol{m} = \boldsymbol{M}/|M|$ is the normalized (reduced) magnetization.
2. The stray field energy density $e_{\mathrm{stray}} = -\boldsymbol{J} \cdot \boldsymbol{H}_{\mathrm{d}}/2$ is connected with the magnetostatic interaction between the magnetic moments. The stray field $\boldsymbol{H}_{\mathrm{d}}$ is the field that results from the dipolar fields of all the magnetic moments in the sample.
3. The Zeeman term $e_{\mathrm{ext}} = -\boldsymbol{J} \cdot \boldsymbol{H}_{\mathrm{ext}}$ describes the influence of an external field. The magnetization tends to align parallel to the applied field.
4. In crystalline materials the energy of the magnetic structure depends on the direction of the magnetization with respect to the crystalline axes. In the simplest form, the magnetocrystalline anisotropy energy density is $e_{\mathrm{ani}} = K_{\mathrm{u}}\sin^2\alpha$, where $K_{\mathrm{u}}$ is the uniaxial anisotropy constant and $\alpha$ is the angle enclosed between the magnetization and the easy axis.

Static magnetic structures represent a minimum of the total energy of the sample. This is not necessarily a global minimum. In numerical calculations equilibrium magnetization structures can be obtained by minimizing the total energy of the magnet with respect to the discretized directional field of the magnetization.

The magnetization dynamics is governed by the Landau–Lifshitz–Gilbert equation

$$\mathrm{d}\boldsymbol{M}/\mathrm{d}t = -\gamma \boldsymbol{M} \times \boldsymbol{H}_{\mathrm{eff}} + \alpha/M_{\mathrm{s}}(\boldsymbol{M} \times \mathrm{d}\boldsymbol{M}/\mathrm{d}t) \tag{8.1}$$

where $\gamma$ is the gyromagnetic ratio and $\alpha$ is a phenomenological damping constant [23]. The equation describes a combined precession and relaxation motion of the magnetization in an effective field $\boldsymbol{H}_{\mathrm{eff}}$. The effective field contains contributions from the aforementioned energy terms. It is obtained from the local energy density by means of a variational derivative with respect to the magnetization $\mu_0\boldsymbol{H}_{\mathrm{eff}} = -M_{\mathrm{s}}^{-1}\delta e/\delta\boldsymbol{m}$. In dynamic micromagnetic simulations, the Landau–Lifshitz–Gilbert equation is used to calculate the evolution of the magnetization $\boldsymbol{M} = \boldsymbol{M}(\boldsymbol{r}, t)$ in time and space. The temporal evolution of $\boldsymbol{M}$ is important if the magnet is not in an equilibrium. Such a non-equilibrium situation is given, e.g., during the magnetization reversal process in an external field.

In soft-magnetic materials, the exchange constant $\lambda = (2A/\mu_0 M_{\mathrm{s}}^2)^{1/2}$ is an intrinsic material-dependent length scale that (roughly) describes the typical spatial extension of inhomogeneities in the magnetic structure, such as, e.g., domain walls.

### *8.5.2. Computational Micromagnetism with the Finite Element Method*

Generally, analytic solutions of micromagnetic problems are only possible if strong simplifications are assumed. Owing to the tremendous progress in computer speed as well as in numerical techniques in the last years, it has become possible to reliably calculate both static magnetic structures and dynamic magnetization processes in nanoscaled ferromagnetic particles. There are several numerical difficulties involved in micromagnetic simulations, including the accurate and fast calculation of the long-range magnetostatic interaction given by the stray field and the stable integration of the Landau–Lifshitz–Gilbert equation. Over the last years, several techniques have been developed to treat these problems. The finite element method is a particularly powerful tool when micromagnetic problems of particles with curved boundaries are to be solved. The versatility of the finite element method is due to the geometrical flexibility connected with the discretization cells. By using cells of irregular tetrahedral shape, the particle's shape can be approximated particularly well, in contrast to the more frequently used finite-difference schemes, where simulating particles with curved boundaries is problematic [24].

The calculation of the stray field is performed by introducing a scalar magnetic potential $U$. The numerical solution of Poisson's equation $\Delta U = \boldsymbol{\nabla M}$ with accurate consideration of the boundary conditions is obtained using a combination of the finite element method with the boundary element method (FEM/BEM). The stray field is derived from $U$ as a gradient field $\boldsymbol{H}_{\mathrm{d}} = -\boldsymbol{\nabla} U$. A detailed description of this precise and fast method is given elsewhere [25]. A particularly advantageous feature of the FEM/BEM scheme is the possibility of calculating the magnetostatic interaction of separate magnetic particles by simply placing the finite element meshes next to each other, without the need to perform time-consuming calculations of the field in the space between the particles. In the present case, this allows us to simulate the influence of magnetostatic coupling in an array of nanowires.

### *8.5.3. Magnetostatically Coupled Nickel Nanowires*

The magnetic properties of sets of hexagonally ordered nickel nanowires have been simulated by means of micromagnetic finite element modelling [26]. The model has been chosen according to the experimental situation described elsewhere [18]. Several nanowires are placed on a hexagonal array with 100 nm period. The wires' diameter is $d = 40$ nm, and their length is $l = 1$ μm. The saturation polarization is $J_{\mathrm{s}} = 0.52$ T and the exchange constant is $A = 10.5$ pJ/m. The wires are assumed to be amorphous, hence the magnetocrystalline anisotropy is zero, $K_{\mathrm{u}} = 0$ J/m$^3$.

The influence of the magnetostatic interaction on the coercive field of an array of nickel nanowires is illustrated in Figure 8.10b. By placing an increasing number of wires on hexagonal lattice sites, the coercive field is calculated for different numbers of interacting wires. The calculation is performed statically by means of energy minimization. The simulations yield a significant decrease of the coercive field from 145 mT in the case of a single, isolated wire to 115 mT in the case of 16 interacting nanowires. A fully micromagnetic simulation without simplifications can hardly be performed on considerably larger arrays because of the numerical costs. However, the tendency shown in Figure 8.7b is clear: The coercive field of the array is strongly reduced by the magnetostatic interaction. Compared to the small number $N$ of wires considered in the simulation, the experimental situation corresponds rather to the case $N \to \infty$. Although the number of points $N$ is not sufficient here for a convincing extrapolation to infinity, it is evident that the experimentally observed value of the coercive field $\mu_0 H_{\mathrm{c}} \approx 100$ mT can only be

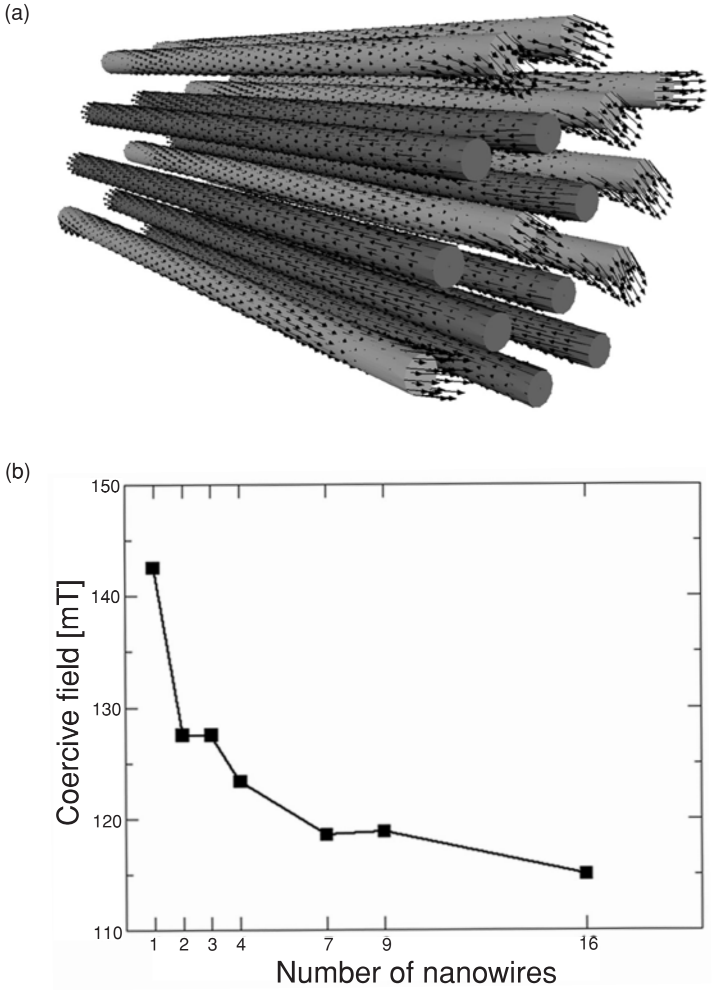

FIGURE 8.10. (a) Micromagnetic simulation of 16 interacting nanowires at the coercive field. Half of the wires have switched in the direction of the field (dark grey). The wires are magnetized homogeneously along the axis. (b) Coercive field of small hexagonal arrays of nanowires as a function of the number of interacting wires.

explained as a consequence of the magnetostatic coupling between the wires. Concerning the magnetic structure of the individual wires, the simulations indicate that the idealized case, according to which the wires are magnetized homogeneously along the wire axis, is fulfilled almost exactly. In an easy-axis hysteresis loop (field applied parallel to the wire axis) the magnetization of each wire is either parallel or anti-parallel to the field. The pronounced magnetostatic shape anisotropy of the wires enforces an alignment of the magnetization parallel to the axis. An example for this is given in Figure 8.10a, where the magnetic structure of a small array consisting of 16 nanowires is displayed. After saturation, the array has been exposed to a reversed field close the coercivity $\mu_0 H_c \approx 115$ mT.

Some wires (dark grey) have switched towards the field; others (light grey) are still aligned anti-parallel to the field. Each wire is a magnetically bi-stable particle.

### *8.5.4. Magnetization Reversal Dynamics in Nickel Nanowires*

To calculate the switching speed and to study the reversal dynamics, micromagnetic simulations based on the Landau–Lifshitz–Gilbert equation have been performed on single nanowires [27]. In all cases, the wires have been exposed instantaneously to a 200 mT field, which is sufficiently strong to revert the magnetization. A Gilbert damping constant $\alpha = 0.1$ is assumed. The dynamic magnetization reversal process of a nickel nanowire of the set discussed above is shown in Figure 8.11a. The reversal begins at the wire's ends. This is where the demagnetizing field has its strongest value.

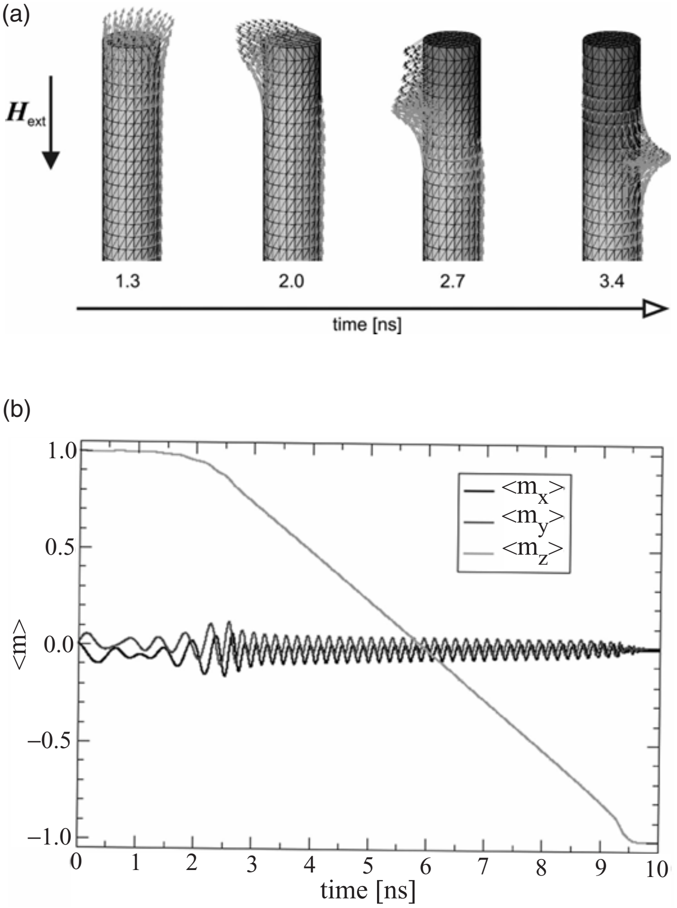

FIGURE 8.11. (a) Snapshots of the initial stages of the magnetization reversal of a Ni nanowire ($d = 40$ nm) via the transverse wall mode. The magnetization reverts in a nucleation-propagation process that starts at the wire's ends. The transverse component of the 180° head-to-head wall precesses in the external field and leads to a spiralling motion of the wall. (b) Average magnetization components along the axis ($m_z$) and perpendicular to it ($m_x$, $m_y$) as a function of time during the reversal.

The demagnetizing field adds to the externally applied field, thus facilitating the magnetization reversal. The nucleated domain, in which the magnetization has switched, is separated from the non-reversed part of the wire by a 180° head-to-head wall [28,32,33]. As the domain wall propagates along the wire axis, the reversed domain expands until the entire sample is switched. In the middle of the domain wall, the magnetization points perpendicular to the wire axis. Since the field is applied along the wire axis, a strong torque is exerted on the magnetization in this region of the domain wall. This leads to a precessional motion of the magnetization in the domain wall, which proceeds on a characteristic spiralling orbit along the wire axis. This motion reflects in oscillations of the magnetization components perpendicular to the wire axis, see Figure 8.11b.

The magnetic structure in this wire is one-dimensional during the reversal, i.e., the direction of the magnetization depends only on the position along the wire axis. It is homogeneous on any cross-section through the wire. Obviously, this case is only realized in very thin wires. As the wire thickness increases, the magnetic structure that is formed during the reversal process becomes three-dimensional. An example for a three-dimensional reversal mode is shown in Figure 8.12a, where the initial stages of a switching process in a slightly thicker nickel nanowire (diameter: 60 nm) are displayed.

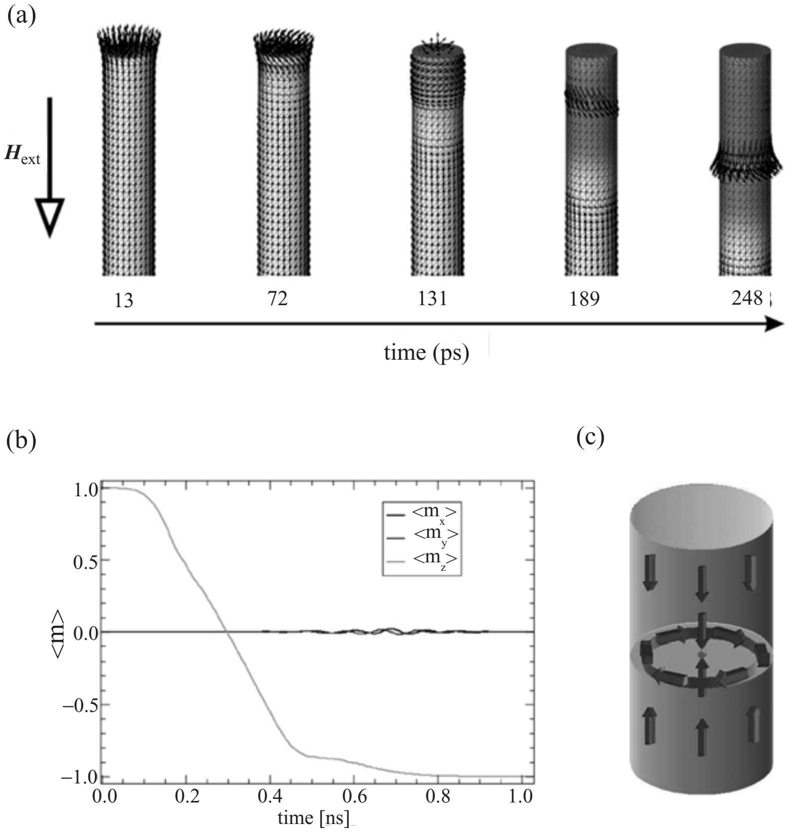

FIGURE 8.12. (a) Magnetization reversal in a Ni nanowire ($d = 60$ nm) via the vortex mode. This reversal process is considerably faster than the transverse mode (b). The switching is accomplished by the nucleation and subsequent propagation of an axial vortex wall. (c) Schematic representation of the vortex wall with a singularity in the middle.

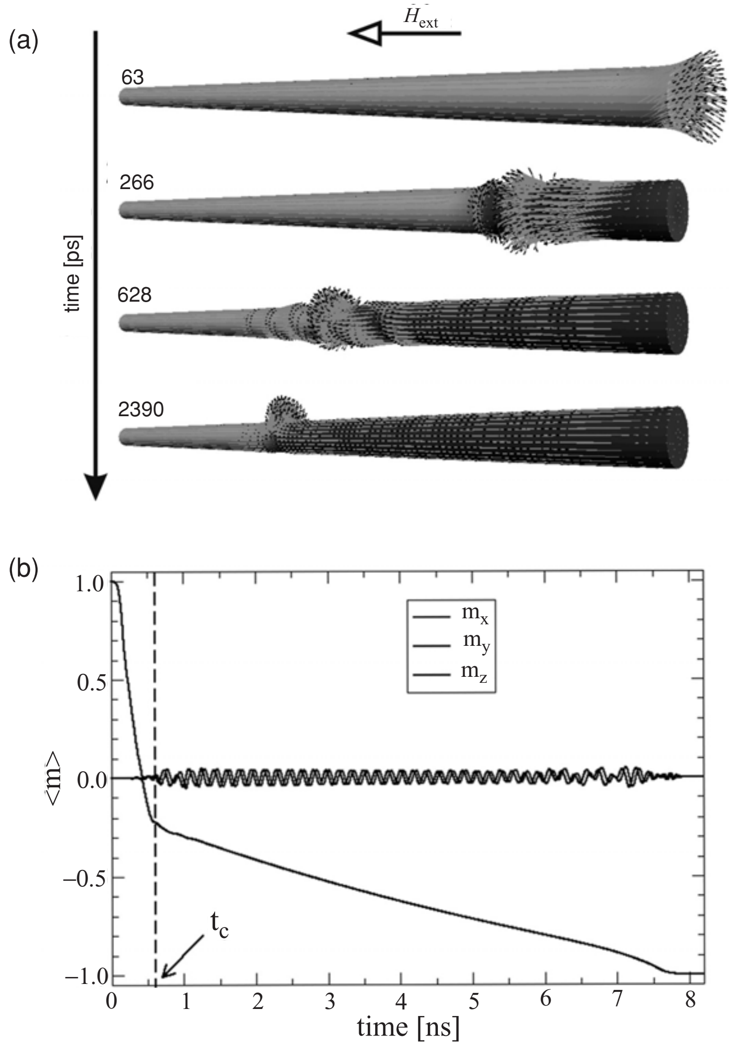

FIGURE 8.13. (a) Dynamic mode conversion in a cone-shaped wire of 1 μm length and linearly varying diameter between 30 and 60 nm. The reversal starts at the thicker end as a vortex mode. The reversal front propagates along the wire. When it passes through a range of critical thickness, the vortex mode converts into the corkscrew mode. (b) Average magnetization components during the reversal of the cone-shaped particle. The mode conversion sets in at the time $t_c$. At that point, the slope of $m_z$ changes drastically, indicating the conversion of the fast vortex reversal mode into the slow corkscrew mode. The conversion into the corkscrew mode also reflects in the onset of the characteristic oscillations in the $m_x$ and $m_y$ components.

The reversal mechanism is again a nucleation-propagation process that starts at the wire's ends. But now the reversed region is separated from the non-reversed region by a vortex wall. The structure of a vortex wall is sketched in Figure 8.12c. It is interesting to note that this structure contains a micromagnetic singularity, known as Bloch point [17,29]. This vortex reversal process has some similarities with the classical curling reversal mode [21,30]. The main difference is the localization of the mode [20]. This reversal process is considerably faster than the aforementioned mode with a propagating transverse domain wall, cf. Figures 8.11b and 8.12b. Hence, the wires should not be too thin if they are to be switched quickly.

The thickness-dependent transition from the vortex wall reversal mode to the transverse wall mode can be nicely simulated in a cone-shaped wire [31]. Figure 8.13a shows an example of the magnetization reversal in a Ni wire with linearly varying thickness ($d = 30$ nm on one end and $d = 60$ nm on the opposite end). The reversal begins with the vortex mode at the thicker end. As the vortex wall proceeds along the wire axis, it passes through regions of constantly decreasing diameter. When the reversal front reaches a region of critical thickness (here $t_c \approx 42$ nm), a spontaneous mode conversion occurs. The mode conversion is clearly visible when the average magnetization components are plotted as a function of time, as shown in Figure 8.13b. At the beginning, the reversal proceeds quickly via the vortex reversal mode (steep slope of the $m_z$ component, $z$ = wire axis). After the conversion into the transverse wall mode, the $m_z$-slope changes abruptly, and the reversal speed is strongly reduced. In this case, about 90% of the switching time is required for the last 30% of the reversal. Besides the change in reversal speed, another effect connected with the mode conversion is the onset of the oscillations in the $m_x$ and $m_y$ components with the beginning of the transverse wall reversal mode.

## 8.6. CONCLUSION

The measurement of the bulk-magnetic properties shows a strong magnetic anisotropy along the nickel column axes, coercive fields of 1200 Oe and nearly 100% squareness. In the demagnetized state the nanowire array exhibits a labyrinth-like domain pattern. Good agreement between the MFM investigation in the presence of an external magnetic field and the hysteresis loop was obtained. Each magnetic pillar is a single-domain magnetic particle, magnetized perpendicular to the template surface and, in principle, can store one bit of information. By using imprint lithography perfectly arranged nickel nanowire arrays have been fabricated. The properties of the magnetic arrays depend on the ordering degree of the nanowire arrangement. If the deviation of the nanowire diameter decreases and the ordering degree of the nanowires array is enhanced, the anisotropy of the whole nanowire array increases. Micromagnetic simulations show that the magnetostatic interaction between the wires has a decisive influence on the coercive field of a nanowire array. Good agreement with the experiment is obtained by simulating an array of 16 interacting wires. Simulations of the magnetization reversal dynamics in single nanowires predict that the magnetization can switch via two different nucleation-propagation modes. Which of the mode occurs depends on the wire thickness. The transverse mode that occurs in thinner wires ($d \approx 30$ nm) leads to a considerably slower reversal than the vortex mode found in thicker wires ($d \approx 60$ nm).

## ACKNOWLDGEMENTS

We are grateful to T. Schweinböck, H. Kronmüller, S. F. Fischer, D. Weiss, D. Navas and M. Vazquez for support, experimental measurements or fruitful discussions. We also like to thank Professor U. Gösele and Professor J. Kirschner for supporting this activity.

# REFERENCES

[1] R. O'Barr, S.Y. Yamamoto, S. Schultz, W. Xu and A. Scherer, J. Appl. Phys. **81**, 4730 (1997).

[2] C.A. Ross, H.I. Smith, T.A. Savas, M. Schattenberg, M. Farhoud, M. Hwang, M. Walsh, M.C. Abraham and R.J. Ram, J. Vac. Sci. Technol. B **17**, 3159 (1999).

[3] D. Routkevitch, A.A. Tager, J. Haruyama, D. Almawlawi, M. Moskovits and J.M. Xu, IEEE Trans. Electron Devices **147**, 1646 (1996).

[4] M.P. Kaneko, IEEE Trans. Magn. **17**, 1468 (1981).

[5] D. Al Mawlawi, N. Coombs and M. Moskovits, J. Appl. Phys. **69**, 5150 (1991).

[6] L. Feiyue, R.M. Metzger and W.D. Doyle, IEEE Trans. Magn. **33**, 3715 (1997).

[7] G.J. Strijkers, J.H.J. Dalderop, M.A.A. Broeksteeg, H.J.M. Swagten and W.J.M. de Jonge, J. Appl. Phys. **86**, 5141 (1999).

[8] H. Zeng, M. Zheng, R. Skomski, D.J. Sellmyer, Y. Liu, L. Menon and S. Bandyopadhyay, J. Appl. Phys. **87**, 4718 (2000).

[9] H. Masuda and K. Fukuda, Science **268**, 1466 (1995).

[10] A.-P. Li, F. Müller, A. Birner, K. Nielsch and U. Gösele, J. Appl. Phys. **84**, 6023 (1998).

[11] K. Nielsch, J. Choi, K. Schwirn, R.B. Wehrspohn and U. Gösele, Nano Lett. **2**, 677 (2002).

[12] A.P. Li, F. Müller and U. Gösele, Electrochem. Soc. Lett. **3**, 131 (2000).

[13] H. Masuda, H. Yamada, M. Satoh, H. Asoh, M. Nakao and T. Tamamura, Appl. Phys. Lett. **71**, 2770 (1997).

[14] K. Nielsch, F. Müller, A.P. Li and U. Gösele, Adv. Mater. **12**, 582 (2000).

[15] J. Choi, K. Nielsch, M. Reiche, R.B. Wehrspohn and U. Gösele, J. Vac. Sci. Technol.B **21**, 763 (2003).

[16] K. Nielsch, F. Müller, R.B. Wehrspohn, U. Gösele, S.F. Fischer and H. Kronmüller, *The Electrochemical Society Proceedings Series*, PV 2000-8, Pennington, NJ, 2000, p. 13.

[17] E. Feldtkeller, Z. Angew. Phys. **19**, 530 (1965).

[18] K. Nielsch, R. Wehrspohn, J. Barthel, J. Kirschner, U. Gösele, S.F. Fischer and H. Kronmüller, Appl. Phys. Lett. **79**, 1360 (2001).

[19] K. Ounadjela, R. Ferré, L. Louail, J.M. George, J.L. Maurice, L. Piraux and S. Dubois, J. Appl. Phys. **81**, 5455 (1997).

[20] H.B. Braun, J. Appl. Phys. **85**, 6172 (1999).

[21] A. Aharoni, *Introduction to the Theory of Ferromagnetism*, Oxford Science Publications, Clarendon Press, Oxford, 1996.

[22] W.F. Brown, Jr., *Micromagnetics*, Interscience Publishers, John Wiley & Sons, New York, London, 1963.

[23] T.L. Gilbert, Phys. Rev. **100**, 1243 (1955).

[24] C.J. Garcia-Cervera, Z. Gimbutas and Weinan E, J. Comp. Phys. **184**, 37 (2003).

[25] D.R. Fredkin and T.R. Koehler, IEEE Trans. Magn. **26**, 415 (1990).

[26] R. Hertel, J. Appl. Phys. **90**, 5752 (2001).

[27] R. Hertel, J. Magn. Magn. Mater. **249**, 251 (2002).

[28] R.D. McMichael and M.J. Donahue, IEEE Trans. Magn. **33**, 4167 (1997).

[29] R. Hertel and H. Kronmüller, J. Magn. Magn. Mater. **238**, 185 (2002).

[30] E.H. Frei, S. Shtrikman and D. Treves, Phys. Rev. **106**, 446 (1957).

[31] R. Hertel and J. Kirschner, Physica B **343** (2004) 206.

[32] D. Hinzke and U. Nowak, J. Magn. Magn. Mater. **221**, 365 (2000).

[33] H. Forster, T. Schrefl, D. Suess, W. Scholz, V. Tsiantos and J. Fidler, J. Appl. Phys. **91**(10), 6914 (2002).